


SCIENTIFIC REPORTS



OPEN

Strain-tuned enhancement of ferromagnetic T_C to 176 K in Sm-doped BiMnO_3 thin films and determination of magnetic phase diagram

Received: 10 November 2016

Accepted: 30 January 2017

Published: 03 March 2017

Eun-Mi Choi, Josée E. Kleibeuker & Judith L. MacManus-Driscoll

BiMnO_3 is a promising multiferroic material but its ferromagnetic T_C is well below room temperature and the magnetic phase diagram is unknown. In this work, the relationship between magnetic transition temperature (T_C) and the substrate induced (pseudo-) tetragonal distortion (ratio of *out-of-plane* to *in-plane* lattice parameters, c/a) in BiMnO_3 thin films, lightly doped to optimize lattice dimensions, was determined. For $c/a > 0.99$, hidden antiferromagnetism was revealed and the magnetisation versus temperature curves showed a tail behaviour, whereas for $c/a < 0.99$ clear ferromagnetism was observed. A peak T_C of up to 176 K, more than 70 K higher than for bulk BiMnO_3 , was achieved through precise strain tuning. The T_C was maximised for strong tensile *in-plane* strain which produced weak octahedral rotations in the *out-of-plane* direction, an orthorhombic-like structure, and strong ferromagnetic coupling.

Strong coupling between magnetism and ferroelectricity in perovskite oxides (ABO_3) has drawn increasing interest because of the potential for magnetoelectric devices for highly sensitive magnetic sensors and low energy random access memory (RAM). BiMnO_3 (BMO) has been extensively investigated because it is one of the rare multiferroics that possesses both ferromagnetism (FM) and ferroelectricity (FE). However, its maximum reported magnetic transition temperature, T_C , is only $\sim 100 \text{ K}^{1,2}$. In addition, recent theoretical and experimental studies have shown that bulk BMO has a centrosymmetric monoclinic structure ($C2/c$) which means the ground state of BMO is not ferroelectric (FE)³. Solovyev *et al.* proposed that hidden antiferromagnetic (AFM) ordering is responsible for the ferroelectricity⁴. These studies have shown the potential of BMO to be a multiferroic, but the combination of strong FM and FE are difficult to achieve.

The magnetic behaviour of BMO is complex owing to competition between FM and AFM coupling. The $6s^2$ lone pair character of Bi^{3+} results in a much higher Jahn-Teller (JT) structural distortion than, for example, in A-type AFM LaMnO_3 (LMO)^{5–10}. According to the Goodenough-Kanamori rules, this distortion breaks the degeneracy of the e_g orbitals as shown in Fig. 1a. The half-filled d_{z^2} ($d_{3z^2-r^2}$) orbitals point towards the empty $d_{x^2-y^2}$ ($d_{3x^2-r^2}/d_{3y^2-r^2}$) orbitals on the next manganese and such interactions are ferromagnetic. In addition, the superexchange interaction between Mn^{3+} ions becomes antiferromagnetic when both e_g orbitals point perpendicular to the bond direction despite the interaction between d_{z^2} and $d_{x^2-y^2}$ orbitals. On the other hand, the ferromagnetic interaction occurs if one of the e_g orbitals points along the bond direction⁹. In BMO, the interaction between the d_{z^2} and $d_{x^2-y^2}$ orbitals happens along both *in-plane* and *out-of-plane* directions and leads to three-dimensional (3D) ferromagnetic interactions (see Fig. 1b). However, there are also AFM interactions along the *ab-plane* (*in-plane*) direction^{7–10}. The special e_g orbital ordering in BMO is caused by the $6s^2$ lone pair character of Bi^{3+} that leads to A cations displacements along the $\langle 111 \rangle$ direction¹⁰. The 3D magnetic interactions in BMO are very different to LMO where ferromagnetic planes alternate antiferromagnetically along *out-of-plane* (A-type AFM).

Department of Materials Science, University of Cambridge, 27 Charles Babbage Road, Cambridge, CB3 0FS, UK. Correspondence and requests for materials should be addressed to E.-M.C. (email: emc63@cam.ac.uk)

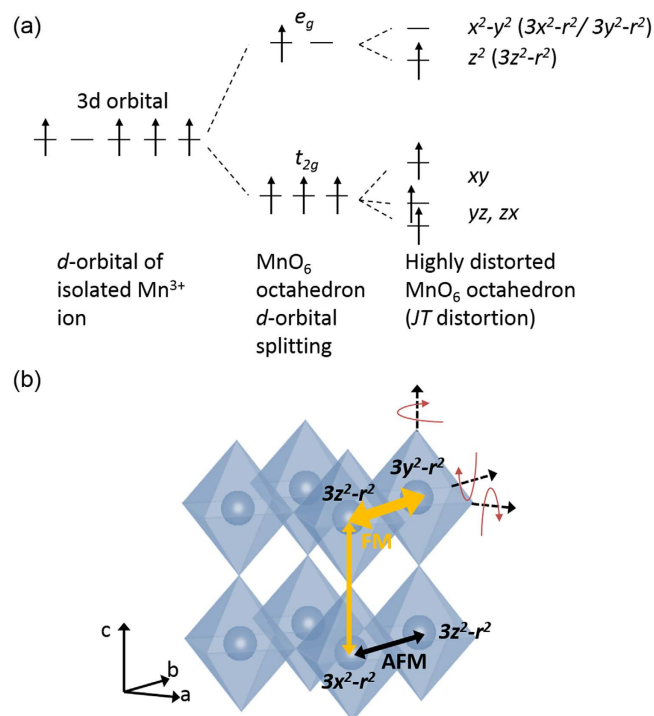


Figure 1. (a) Splitting in energy of the d -orbitals of Mn^{3+} due to the MnO_6 octahedron and the further Jahn-Teller distortion (b) Schematic illustration of the magnetic interactions of Mn^{3+} ions with e_g orbitals within MnO_6 octahedra in BiMnO_3 . The Bi^{3+} ions at the A-site are not shown. Oxygen is at the corners of the octahedra. Yellow arrows and black arrows indicate ferromagnetic and antiferromagnetic superexchange interactions, respectively. The thickness of arrows indicates the strength of the couplings. Red arrows show MnO_6 octahedral rotations.

Strain in the structure (whether induced isostatic pressure applied to bulk samples or biaxial pressure applied in thin films by heteroepitaxial growth) can cause octahedral rotations that change the Mn-O-Mn bond lengths and angles. The 3D magnetic state of BMO is very sensitive to changes in Mn-O-Mn bond lengths and angles. Even as low as a $\sim 1^\circ$ bond angle change radically alters the magnetic properties⁷. Overall, long-range FM coupling dominates over AFM coupling, but ‘hidden’ AFM remains and is revealed under certain strain conditions^{7,8,11}. This explains why T_C s of between 50 and 100 K have been observed when films are grown on different substrates^{12–14}. Therefore, precise tuning of the Mn-O-Mn bond lengths and angles is critical for engineering the FM properties. It should be noted, however, that when the FM properties are optimised, the FE properties are not necessarily optimised^{1,11,13,15–17}.

Recently, the improved multiferroic properties of BMO thin films by independently tuning the *in-plane* and *out-of-plane* bond lengths, using a combination of isostatic chemical pressure and biaxial mechanical pressure were demonstrated. The chemical pressure was induced by low-level Sm doping of the A-site to decrease the overall cell volume and the biaxial mechanical pressure was induced using epitaxial strain. The contraction of the BiMnO_3 lattice with Sm, together with the *in-plane* lattice extension by growth on SrTiO_3 ($a = 3.905 \text{ \AA}$) enabled optimization of both the *in-plane* and *out-of-plane* lattice dimensions. An enhancement of FM interactions in the *out-of-plane* direction by reducing the *out-of-plane* lattice parameter and a reduction of AFM interactions *in-plane* by increasing the *in-plane* lattice parameter were shown. An increase in the T_C to 140 K was achieved, as well as FE behaviour at room temperature (RT). However, since the aim of the earlier work was to measure FE properties, the films were grown relatively thick ($\sim 200 \text{ nm}$), in order for the FE leakage to be minimised, and so uniform straining of the $\text{Bi}_{1-x}\text{Sm}_x\text{MnO}_3$ ($x = 0.15$, BSMO) film was lost. Consequently, a range of strain states in the films meant that large AFM component remained in the films and a strong tail behaviour in the magnetic transition was observed together with an AFM transition at $\sim 30 \text{ K}$, indicating the competition between the AFM and FM interactions^{9,11,13,18,19}. This result is in agreement with the suggestion that hidden AFM ordering is responsible in FE materials⁴.

The main aim of this work is to achieve a range of different strain states in BSMO thin films so as to determine the conditions for optimising its magnetic properties, i.e. to minimise the AFM component and maximise the FM component. A secondary aim is to shed light on the magnetic phase diagram. The ferroelectric properties of the very thin films of this work were not measured. This is because thin film oxide perovskite ferroelectrics (no matter their composition) show leaky behaviour, and the 20 nm BSMO films studied here are no exception. Also, the bottom electrode, SrRuO_3 , which would need to be used on the different insulating substrates, may induce unexpected octahedral rotations in the BSMO films²⁰. On the other hand, we have already demonstrated that relatively thick BSMO films grown on SrTiO_3 show excellent ferroelectric properties at RT¹⁸. Further work

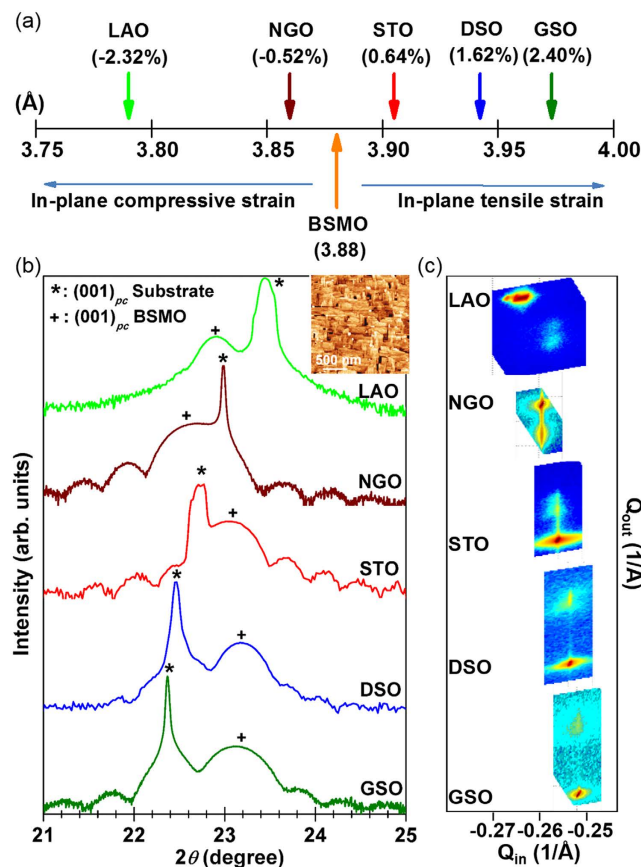


Figure 2. (a) Lattice mismatch between BSMO and the various substrates at RT. XRD spectra of ~ 20 nm thick BSMO films grown on the various substrates; (b) The BSMO (001) peak and substrate peak are marked by (+) and (*), respectively. Reflections are indexed based on pseudo-cubic symmetry. The inset shows an atomic force microscopy image with $2 \times 2 \mu\text{m}^2$ for BSMO grown on STO. The root-mean-square (RMS) roughness of the film was ~ 0.26 nm. (c) RSMs around the (332) peak of DSO, GSO and NGO, and (103) of STO and LAO. The substrate peaks are the sharper, red-centred, high intensity peaks which appear at the bottom of the RSM plots, except for LAO and NGO.

is required to measure the FE properties without changing the octahedral rotations from SrRuO₃ (or any other bottom electrode film), for example by using second-harmonic generation studies of films grown directly on insulating substrates.

Very thin films (~ 20 nm) of BSMO were grown on a range of different substrates. It was necessary to grow very thin films (~ 20 nm) to provide a near-uniform strain state. The structural distortion of the films was measured using conventional x-ray diffraction (XRD). This gives an indirect assessment of the octahedral rotations: the further the (pseudo-) tetragonal distortion (c/a) is from 1, the greater level of rotation^{20–23}. While synchrotron XRD would be optimum to determine bond angles^{21,22}, these measurements were not performed here since the aim of work to demonstrate property enhancement through careful materials engineering.

The key finding of our work is that by engineering an optimal structural distortion into BSMO films, enhanced FM T_C 's with clear transitions, up to 176 K, can be achieved. At the same time, by engineering a range of structural distortions into films, the magnetic phase diagram was determined.

Two different experiments were undertaken. The first one explored the magnetic properties of the films of constant thickness (20–24 nm) on substrates with different lattice mismatch. Thicknesses of ~ 20 nm were low enough to give coherent growth with little relaxation of strain but thick enough to give a sizeable magnetic signal. The second study focused on the magnetic properties of films of a range of thicknesses (10, 20 and 200 nm) grown on SrTiO₃ (STO). Films were grown on orthorhombic, paramagnetic (110) DyScO₃ (DSO), (110) GdScO₃ (GSO), (110) NdGaO₃ (NGO) substrates, on cubic, non-magnetic (001) TiO₂-terminated STO, and on rhombohedral, non-magnetic (001) LaAlO₃ (LAO) substrates. All substrates were thermally treated to show well defined terraces before deposition. The lattice mismatch values between the BSMO and the various substrates are shown in Fig. 2a. BSMO lattice parameter is assumed from a pseudo-cubic cell volume of 58.8 \AA^3 ^{18,24,25}.

Results and Discussion

Figure 2b shows $2\theta - \omega$ XRD patterns of 20–24 nm BSMO films grown on the various substrates. The films were fully epitaxial and no impurity phases were observed (Fig. 2b). Clear thickness fringes for all these films were observed (except for LAO), indicating the high crystal quality. From NGO to GSO, the (001)_{pc} peak of the BSMO

Substrate	In-plane lattice parameter Substrate [Å]	Lattice mismatch (%)	In-plane lattice parameter BSMO (Å)	Out-of-plane lattice parameter BSMO [Å]	Pseudo-cubic unit cell volume [Å ³]	(Pseudo-) Tetragonal distortion, c/a	Crystal Structure BSMO	T_C (K)	M_r (μ_B/Mn) at 10 K
LAO(001)	3.790	-2.32	3.89 ± 0.005	3.88 ± 0.005	58.7 ± 0.2	0.997 ± 0.005	Tetragonal	95 ± 10	0.10
NGO(110) ^a	3.864	-0.52	3.86 ± 0.005	3.93 ± 0.005	58.6 ± 0.2	1.018 ± 0.005	Orthorhombic	100 ± 6	0.11
STO (001)	3.905	0.64	3.90 ± 0.005	3.845 ± 0.005	58.6 ± 0.2	0.984 ± 0.005	Tetragonal	150 ± 3	0.12
DSO(110) ^a	3.943	1.62	3.94 ± 0.005	3.81 ± 0.005	59.1 ± 0.2	0.967 ± 0.005	Orthorhombic	160 ± 3	0.18
GSO(110) ^a	3.973	2.40	3.97 ± 0.005	3.83 ± 0.005	60.4 ± 0.2	0.965 ± 0.005	Orthorhombic	83 ± 3	0.06

Table 1. Pseudo-cubic unit cell lattice parameters, lattice mismatch, unit cell volume, (pseudo-) tetragonal distortion, crystal structure, magnetic transition temperature (T_C) and remanent magnetic moment (M_r) at 10 K of ~20 nm BSMO thin films grown on various substrates. ^aAverage pseudo-cubic *in-plane* lattice parameter of orthorhombic structure determined from the RSMs.

shifts to a higher 2θ angle indicating a reduction of the *out-of-plane* lattice parameter, which is consistent with the *in-plane* strain becoming more tensile across the series, as expected. The inset of Fig. 2b shows an AFM height image of a typical film grown on STO. A homogeneous surface morphology of aligned rectangular faceted grains was observed.

Figure 2c shows reciprocal space maps (RSMs) around the (332) peak of DSO, GSO and NGO, and (103) of STO and LAO. The coincidence of the substrate and film *in-plane* reciprocal lattice vector values (Q_{in}) from NGO to GSO indicates that the films are fully *in-plane* strained to the substrates. The shift of the film peaks to higher Q_{in} values indicates an increase of the *in-plane* lattice parameter which is expected as the substrate lattice parameter increases (Fig. 2c). On the other hand, consistent with Fig. 2b, the *out-of-plane* reciprocal lattice vector (Q_{out}) shifts to higher values as the substrate lattice parameters increase. The film on LAO is fully relaxed, showing that the growth is incoherent for such large *in-plane* compressive substrate strain (-2.32%). This also explains the absence of thickness fringes in the *out-of-plane* spectra for BSMO on LAO (Fig. 2b).

A summary of lattice parameters, cell volumes, (pseudo-)tetragonal distortions (the ratio between *out-of-plane* and *in-plane* lattice parameters, c/a), crystal structures, FM transition temperatures (T_C) and remanent magnetic moment (M_r) of the ~20 nm BSMO films are shown in Table 1.

For all the films, the BSMO cell volume is significantly reduced compared to the bulk BMO value of 61.5 \AA^3 . This is consistent with the partial replacement of Bi^{3+} by the smaller Sm^{3+} ion¹⁸. Except for BSMO on GSO ($60.4 \pm 0.2 \text{ \AA}^3$), the pseudo-cubic cell volume of all the BSMO films was around $58.8 \pm 0.3 \text{ \AA}^3$. The increase in unit-cell volume on GSO is likely due to the large biaxial tensile *in-plane* strain (+2.4%), which cannot be compensated for by elastically reducing the *out-of-plane* lattice parameter to such a large extent, and so instead other *out-of-plane* strain relaxation mechanisms must come into play, e.g. compositional modification such as oxygen loss or cation non-stoichiometry. This is in contrast with BSMO on LAO. Here, there is a similar strain level but it is of opposite sign (-2.32%). Unlike BSMO on LAO, GSO can maintain *in-plane* straining because it is possible to strengthen the Mn-O-Mn bonds. On the other hand, for the films on LAO, it is not possible to decrease the (Mn-O-Mn) angle sufficiently to accommodate the *in-plane* strain.

For NGO, STO and DSO substrates which produce more moderate *in-plane* strain, cf. LAO or GSO, the *out-of-plane* lattice parameters are increasingly reduced across the series, as the *in-plane* lattice parameter is increased. This is as expected from simple elastic deformation arguments. The crystal structures of the BSMO films were determined from the asymmetric RSMs at various ϕ -angles (See Fig. 2c, and Supporting Information). The films on STO and LAO were found to be tetragonal, while the films on DSO, GSO and NGO had an orthorhombic-like structure.

To investigate the effect of biaxial strain on the magnetic properties of the BSMO films, field cooled $M - T$ measurements were undertaken. Herein, normalised $M - T$ curves are shown because these are measured under two different conditions: BSMO on STO and LAO were measured at a field of 200 Oe whereas $M - T$ curves of BSMO on DSO, GSO and NGO were measured at 0 Oe after field cooling at 1 T. The two conditions were necessary because of very high paramagnetic background of DSO, GSO and NGO substrates. For the same reason, magnetic hysteresis curves are not shown. Instead, in Table 1, M_r at 10 K is shown for the different films.

Figure 3 shows the $M - T$ curves of the BSMO films on the various substrates. The data can be separated into two different types of curve. The first type shows a tail behaviour. This is found for BSMO on LAO and NGO. Such a behaviour has been reported before for BMO films and indicates the competition between AFM and FM interactions^{9,11,13,19}. When the AFM interactions become dominant, the tail behaviour becomes stronger¹⁹. In addition to the tail behaviour, the BSMO films on LAO and NGO substrates also show clear AFM transitions at ~30 K, which means the hidden AFM is revealed at low temperature¹⁸.

The second type of curve shows a clear FM transition and no tail behaviour. This was the case for BSMO on STO, DSO and GSO. Here, T_C s ranged from 80 K on GSO to 160 K on DSO, the latter value being enhanced by 60 K compared to strained BMO films^{13,14}. For BSMO on DSO and GSO, the magnetic moments increase at low temperature in spite of the clear FM transitions being observed. This is not consistent with a standard FM feature where the magnetic moment saturates at low temperature. The results indicate the presence of AFM coupling²⁶⁻²⁸. For BSMO on STO, a ferromagnetic transition at 150 K is observed with a clear AFM transition at ~30 K also observed. The explanation of these two different magnetic behaviours is discussed later.

To understand the relation between magnetic behaviour and strain, T_C and T_N are plotted versus the (pseudo-) tetragonal distortion (c/a), as shown in Fig. 4. A clear and very sensitive relationship between the magnetic behaviour of BSMO and the (pseudo-) tetragonality of the unit cell is observed. First of all, for $c/a < 0.99$, a clear FM

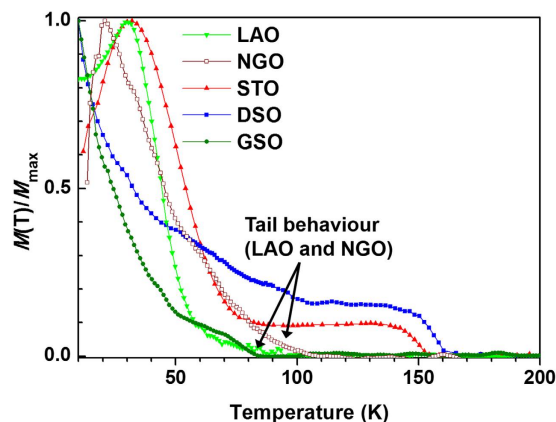


Figure 3. The temperature dependence of magnetisation ($M - T$) for ~ 20 nm BSMO films grown on various substrates. The normalized *in-plane* $M - T$ curves of BSMO on STO and LAO were measured at a field of 200 Oe. The $M - T$ curves of BSMO on DSO, GSO and NGO were measured at 0 Oe after field cooling at 1 T. Arrows indicate the tail behaviour present for LAO and NGO substrates.

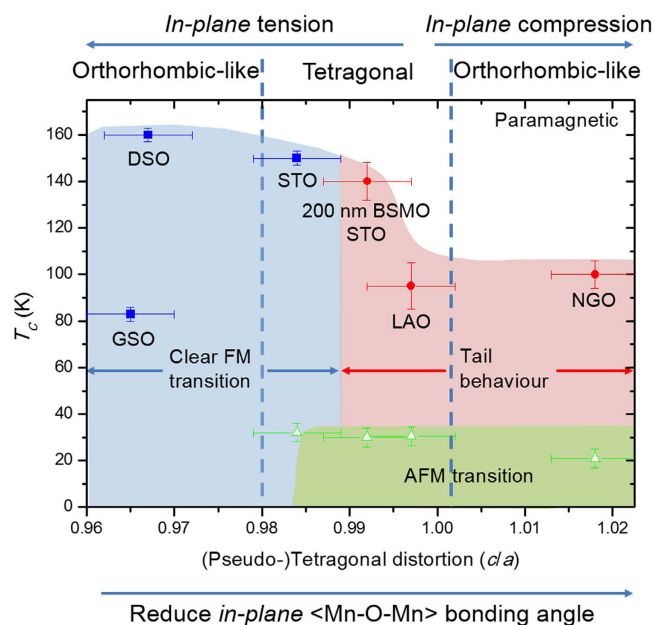


Figure 4. Magnetic phase diagram for BSMO showing the relationship between tetragonality of pseudo-cubic and the magnetic transition temperature based on ~ 20 nm thick BSMO films studied in this paper. The data for 200 nm thick BSMO on STO (from ref. 18) is included to provide more information about the transition region near $c/a \sim 0.99$.

transition without tail behaviour is obtained. For $c/a > 0.99$, hidden AFM is obtained and is manifest as a tail behaviour in the $M - T$ curves. The strong relationship between magnetic structure and c/a is consistent with other manganites^{26,29–33}. For example, for $\text{La}_{0.5}\text{Sr}_{0.5}\text{MnO}_3$, by varying the c/a ratio from 0.97 to 1.06, the magnetic phase changes from A-type AFM to FM to C-type AFM²⁹. According to recent theoretical calculations on LaMnO_3 , an insulating FM phase is formed under small tensile strain whereas a metallic FM phase and an A-type AFM phase is formed under large compressive and tensile strain, respectively³⁴. The sensitivity of the magnetic behaviour with c/a ratio in manganites is caused by the change of the JT distortion of the MnO_6 octahedra and the change of the Mn-O-Mn bond lengths and angles.

To understand why T_c increases when the c/a ratio is reduced, it is necessary to understand more about the precise crystal structure and the MnO_6 octahedral rotations. Minor strained and relaxed BSMO films were found to have a tetragonal crystal structure, indicating either $a^0a^0c^-$ or $a^0a^0c^+$ octahedral rotation patterns (Glazer's notation)³⁵. On the other hand, when the films are grown under large strain, either tensile or compressive, the film crystal structure is orthorhombic-like, as determined by doing x-ray scans around the $(103)_{pc}$ peaks along the four pseudo-cubic *in-plane* directions (see Supporting Information). This indicates that the oxygen octahedra have an $a^-a^-c^+$ rotation pattern.

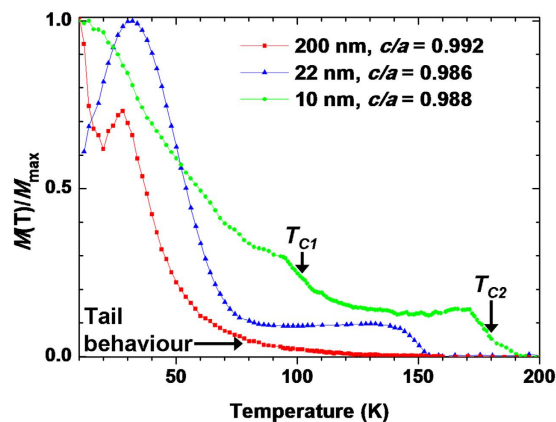


Figure 5. The normalized *in-plane* $M - T$ curves for BSMO thin films on STO with different thickness, 200 (taken from ref. 18), 20 and 10 nm at a field of 200 Oe.

From previous studies of strained oxide perovskites, ABO_3 , the degree of rotation along both the *in-plane* and *out-of-plane* axes depends strongly on the amount and sign of the strain^{20,21}. Hence, under compressive *in-plane* strain ($c/a > 0.98$), there are strong rotations along the *out-of-plane* axis, in combination with weaker rotations along the *in-plane* axis³⁶. Under tensile strain ($c/a < 0.98$), it is the other way around: strong rotations occur along the *in-plane* axes and weaker rotations along the *out-of-plane* axis. The change in rotation patterns and the degree of the rotations impact the $\langle \text{Mn-O-Mn} \rangle$ bond angles and, as a result, the magnetic behaviour.

Taking the above information into account, for strong tensile strained orthorhombic-like BSMO ($c/a < 0.98$), stronger *in-plane* FM interactions are expected (see Fig. 1b) since the *in-plane* bond angles are likely to be relatively close to 180° , as a result of the weak rotations along the *out-of-plane* axis.

Looking at the left hand region of Fig. 4, this is indeed observed, i.e. the high T_C samples show clear FM transitions. The results agree with literature, where rare earth manganites and cobaltites show stronger FM interactions and higher T_C s when the bond angles are close to 180° ^{36,37}.

The highest T_C (~ 160 K) was found for BSMO on DSO ($c/a = 0.967 \pm 0.005$). A reduced T_C of ~ 83 K was found for BSMO on GSO. This film would be expected to have the highest T_C based on it having the lowest c/a ratio. However, it is very likely that this film has an increased defect concentration because of the very large *in-plane* strain which results in a significant increase in the unit-cell volume (Table 1). For the films on DSO and GSO, the *in-plane* FM interaction becomes stronger and dominant, and so the AFM signal becomes relatively weak because the AFM interaction is hidden by the strong FM signal. This is the same situation as in bulk BMO where only FM behaviour is observed. Instead of showing a clear AFM behaviour, i.e. an AFM transition and/or a tail behaviour, the $M - T$ curves for films on DSO and GSO are not saturated at low temperature (see Fig. 3). This lack of saturation is indicated by remanent AFM components, which could originate from a cluster-glass magnetic state²⁸.

Even though there is remanent AFM behaviour, the M_r of BSMO on DSO has the largest value ($\sim 0.18 \mu_B/\text{Mn}$). This is because of a stronger FM behaviour arising from dominant FM interactions. On the other hand, BSMO on GSO has the lowest M_r ($\sim 0.06 \mu_B/\text{Mn}$), consistent with increased defects in the film.

Looking at the middle region ($0.98 < c/a < 1$) of Fig. 4 where there is a low level of *in-plane* tension, the BSMO is tetragonal instead of orthorhombic-like as was observed for high *in-plane* tension ($0.98 < c/a$). Since *in-plane* rotations are absent for this low strain level, there are stronger *out-of-plane* FM interactions, with an *out-of-plane* $\langle \text{Mn-O-Mn} \rangle$ bond angle of 180° . This leads to an intermediate magnetic state and explains why for STO and LAO AFM interactions (at ~ 30 K) are observed in addition to FM interactions (see Fig. 3).

Finally, looking at the right hand region ($c/a > \sim 1$) of Fig. 4 where there is a higher lever of *in-plane* compressive strain, an orthorhombic-like structure is produced once more for BSMO on NGO. Hence, in this region, stronger *out-of-plane* FM interactions and weaker *in-plane* FM interactions are expected. Therefore, the *in-plane* FM interactions do not dominate the magnetic behaviour. As a result, T_C decreases as the c/a ratio is increased, and a clear AFM transition is observed around 30 K, as well as an AFM tail behaviour (see Fig. 3).

Finally, by studying different thickness films on STO, the intermediate transition region ($0.980 < c/a < 0.995$) of Fig. 4 is probed more closely. Figure 5 shows the $M - T$ curves for BSMO films on STO of 200, 20 and 10 nm thickness. The different film thicknesses result in different levels of strain relaxation and hence different c/a ratios. For the 200 nm thick film, the T_C is enhanced to $\sim 140 \pm 6$ K (cf. the bulk BMO T_C of ~ 100 K). Both a tail behaviour and an AFM transition at 30 K are observed but not a clear FM transition. For the 20 nm thick film, a clear FM transition is observed with T_C of 150 ± 3 K. There is no tail behaviour, but there is an AFM transition at ~ 30 K.

For the 10 nm thick film, a clear FM transition is observed with T_C (termed T_{C2}) of 176 ± 3 K. There is no tail behaviour, nor a 30 K AFM transition. However, there is a second FM transition with T_C (termed T_{C1}) at 100 ± 3 K. T_{C2} is surprisingly large, enhanced by ~ 70 K compared to bulk BMO, while T_{C1} is very close to the T_C of bulk BMO. This feature is similar to ultrathin $\text{La}_{0.67}\text{Sr}_{0.33}\text{MnO}_3$ (LSMO) films (< 10 unit cells) where a double transition is found with a much enhanced T_C at ~ 560 K, and a second lower transition at ~ 200 K. Thicker LSMO films (> 20 unit cells), on the other hand, show bulk T_C s of ~ 350 K²⁷. The two ferromagnetic phases for the 10 nm thick BSMO film likely originate from one or more of the possible strain relaxation mechanisms which occur in perovskite films, e.g. phase separation, non-stoichiometry, or deformation of BO_6 octahedra³⁸⁻⁴³.

In conclusion, the relation of magnetic properties and crystal structure in BiMnO₃, the most promising multiferroic with a relatively high FM T_C , was determined for the first time. Sm-doping of the Bi site at a level of 15% was undertaken to reduce the unit cell volume to enhance FM coupling (3D chemical pressure), and different substrates were used (2D biaxial pressure) to expand or contract the unit cell *in-plane*. Hence, 3D + 2D biaxial straining were used *together* to precisely engineer the BiMnO₃ crystal structure, so as to optimise the 3D Mn-O-Mn magnetic coupling. A magnetic phase diagram for the system was mapped out for $0.96 < c < 1.02$. It was possible to eliminate the hidden AFM and strongly increase the T_C by optimizing the (pseudo-)tetragonal distortion (c/a). For $c/a < 0.98$, the films showed a clear FM behaviour. On the other hand, for $c/a > 0.98$, hidden AFM was revealed in addition to the FM behaviour.

With appropriate choice of substrate, doping and film thickness, it was possible to strongly increase T_C . A 10 nm thick Sm-doped BiMnO₃ film grown on STO showed a sharp FM T_C of 176 ± 3 K and a 20 nm thick Sm-doped BiMnO₃ film grown on DSO showed a sharp FM T_C of 160 ± 3 K. Of course, the ultimate goal for BMO films is to achieve both strong FM and FE, and to do this above room temperature. To achieve this, the right strain state needs to be engineered into films thicker than a few 10's of nm, thereby reducing leakage. A possible future approach is to use nanocomposite films where high strain levels can be induced in thick films (>100 nm) and where enhanced FM and FE properties have already been demonstrated in other perovskites⁴⁴.

Methods

Films were grown by pulsed laser deposition (PLD) from a single ceramic target. The growth rate was 0.07–0.08 Å/pulse. For the film growth, the laser pulse rate was 2 Hz with a laser fluence of 1.3 J cm^{-2} . The oxygen pressure was fixed at 100 mTorr and growth temperature was 650 °C. To confirm the phase purity, crystalline quality and the 3D strain state of the films at RT, $2\theta - \omega$ scans and reciprocal space maps (RSMs) were carried out using a Panalytical Empyrean high resolution x-ray diffraction (XRD) system. We determined the *out-of-plane* lattice parameter by measuring the position of the (00 l) peaks in the $2\theta - \omega$ scans as well as the (103) pseudo-cubic (pc) peak of the BSMO in the RSMs. The film thicknesses were determined by x-ray reflectivity. To determine the film surface morphology, atomic force microscopy was performed. The temperature dependence of magnetisation ($M - T$) was determined using a superconducting quantum interference device (SQUID) magnetometer (Quantum Design, MPMS).

References

- Moreira dos Santos, A. *et al.* Evidence for the likely occurrence of magnetoferroelectricity in the simple perovskite, BiMnO₃. *Solid State Commun.* **122**, 49–52 (2002).
- Seshadri, R. & Hill, N. A. Visualizing the Role of Bi 6s “Lone Pairs” in the Off-Center Distortion in Ferromagnetic BiMnO₃. *Chem. Mater.* **13**, 2892–2899 (2001).
- Belik, A. A. Polar and nonpolar phases of BiMO₃: A review. *J. Solid State Chem.* **195**, 32–40 (2012).
- Solovyev, I. V. & Pchelkina, Z. V. Magnetic-field control of the electric polarization in BiMnO₃. *Phys. Rev. B* **82**, 094425 (2010).
- Belik, A. A. *et al.* Origin of the Monoclinic-to-Monoclinic Phase Transition and Evidence for the Centrosymmetric Crystal Structure of BiMnO₃. *J. Am. Chem. Soc.* **129**, 971–977 (2007).
- Pinsard-Gaudart, L. *et al.* Stability of the Jahn-Teller effect and magnetic study of LaMnO₃ under pressure. *Phys. Rev. B* **64**, 064426 (2001).
- Kozlenko, D. P. *et al.* Competition between ferromagnetic and antiferromagnetic ground states in multiferroic BiMnO₃ at high pressures. *Phys. Rev. B* **82**, 014401 (2010).
- Atou, T., Chiba, H., Ohoyama, K., Yamaguchi, Y. & Syono, Y. Structure Determination of Ferromagnetic Perovskite BiMnO₃. *J. Solid State Chem.* **145**, 639–642 (1999).
- Yang, C.-H. *et al.* Orbital ordering and enhanced magnetic frustration of strained BiMnO₃ thin films. *Europhys. Lett.* **74**, 348–354 (2006).
- Moreira Dos Santos, A. *et al.* Orbital ordering as the determinant for ferromagnetism in biferroic BiMnO₃. *Phys. Rev. B* **66**, 064425 (2002).
- Jeen, H. *et al.* Growth and characterization of multiferroic BiMnO₃ thin films. *J. Appl. Phys.* **109**, 074104 (2011).
- Son, J. Y., Kim, B. G., Kim, C. H. & Cho, J. H. Writing polarization bits on the multiferroic BiMnO₃ thin film using Kelvin probe force microscope. *Appl. Phys. Lett.* **84**, 4971 (2004).
- Gajek, M. *et al.* Spin filtering through ferromagnetic BiMnO₃ tunnel barriers. *Phys. Rev. B* **72**, 020406 (2005).
- De Luca, G. M. *et al.* Ferromagnetism and ferroelectricity in epitaxial BiMnO₃ ultra-thin films. *Appl. Phys. Lett.* **103**, 062902 (2013).
- Yang, H. *et al.* Is ferroelectricity in BiMnO₃ induced by superlattice? *J. Mat. Sci.* **43**, 3604 (2008).
- Son, J. Y. & Shin, Y.-H. Multiferroic BiMnO₃ thin films with double SrTiO₃ buffer. *Appl. Phys. Lett.* **93**, 062902 (2008).
- Grizalez, M., Mendoza, G. A. & Prieto, P. Analysis of multiferroic properties in BiMnO₃ thin films. *J. Phys. Conf. Ser.* **167**, 012035 (2009).
- Choi, E.-M. *et al.* Ferroelectric Sm-Doped BiMnO₃ Thin Films with Ferromagnetic Transition Temperature Enhanced to 140 K. *ACS Appl. Mater. Interfaces* **6**, 14836 (2014).
- Hirone, T., Maeda, S., Tsubokawa, I. & Tsuya, N. On the Magnetic Properties of the System MnSb–CrSb. *JPSJ* **11**, 1083–1087 (1956).
- Vailionis, A. *et al.* Misfit strain accommodation in epitaxial ABO₃ perovskites: Lattice rotations and lattice modulations. *Phys. Rev. B* **83**, 064101 (2011).
- May, S. J. *et al.* Quantifying octahedral rotations in strained perovskite oxide films. *Phys. Rev. B* **82**, 014110 (2010).
- Rotella, H. *et al.* Octahedral tilting in strained LaVO₃ thin films. *Phys. Rev. B* **85**, 184101 (2012).
- D. P. Kozlenko, V. P. Glazkov, Z. Jirak & B. N. Savenko, *J. Phys.: Condens. Matter* **16**, 2381–2394 (2004).
- Jia, Y. Q. Crystal radii and effective ionic radii of the rare earth ions. *J. Solid State Chem.* **95**, 184–187 (1991).
- Chiba, H., Atou, T. & Syono, Y. Magnetic and Electrical Properties of Bi_{1-x}Sr_xMnO₃: Hole-Doping Effect on Ferromagnetic Perovskite BiMnO₃. *J. Solid State Chem.* **132**, 139–143 (1997).
- Sadoc, A. *et al.* Large Increase of the Curie Temperature by Orbital Ordering Control. *Phys. Rev. Lett.* **104**, 046804 (2010).
- Boschker, H. *et al.* High-Temperature Magnetic Insulating Phase in Ultrathin La_{0.67}Sr_{0.33}MnO₃ Films. *Phys. Rev. Lett.* **109**, 157207 (2012).
- Fertman, E. *et al.* Exchange bias in phase-segregated Nd_{2/3}Ca_{1/3}MnO₃ as a function of temperature and cooling magnetic fields. *J. Appl. Phys.* **115**, 203906 (2014).
- Fang, Z., Solovyev, I. V. & Terakura, K. Phase Diagram of Tetragonal Manganites. *Phys. Rev. Lett.* **84**, 3169 (2000).
- Suwardi, A. *et al.* Turning antiferromagnetic Sm_{0.34}Sr_{0.66}MnO₃ into a 140 K ferromagnet using a nanocomposite strain tuning approach. *Nanoscale* **8**, 8083 (2016).

31. Nanda, B. R. K. & Satpathy, S. Effects of strain on orbital ordering and magnetism at perovskite oxide interfaces: LaMnO₃/SrMnO₃. *Phys. Rev. B* **78**, 054427 (2008).
32. Solovyev, I. V. & Terakura, K. Spin canting in three-dimensional perovskite manganites. *Phys. Rev. B* **63**, 174425 (2001).
33. Baena, A., Brey, L. & Calderón, M. J. Effect of strain on the orbital and magnetic ordering of manganite thin films and their interface with an insulator. *Phys. Rev. B* **83**, 064424 (2011).
34. Hou, Y. S., Xiang, H. J. & Gong, X. G. Intrinsic insulating ferromagnetism in manganese oxide thin films. *Phys. Rev. B* **89**, 064415 (2014).
35. Glazer, A. M. The classification of tilted octahedra in perovskites. *Acta Cryst. B* **28**, 3384 (1972).
36. Fuchs, D. *et al.* Tuning the magnetic properties of LaCoO₃ thin films by epitaxial strain. *Phys. Rev. B* **77**, 014434 (2008).
37. Kajimoto, R. *et al.* R-Dependence of Spin Exchange Interactions in RMnO₃ (R = Rare-Earth Ions). *J. Phys. Soc. Jpn.* **74**, 2430 (2005).
38. Bibes, M. *et al.* Nanoscale Multiphase Separation at La_{2/3}Ca_{1/3}MnO₃/SrTiO₃ Interfaces. *Phys. Rev. Lett.* **87**, 067210 (2001).
39. Wimbush, S. C. *et al.* Interfacial Strain-Induced Oxygen Disorder as the Cause of Enhanced Critical Current Density in Superconducting Thin Films. *Adv. Funct. Mater.* **19**, 835–841 (2009).
40. Gazquez, J. *et al.* Lattice mismatch accommodation via oxygen vacancy ordering in epitaxial La_{0.5}Sr_{0.5}CoO_{3-δ} thin films. *APL Mater.* **1**, 012105 (2013).
41. Vailionis, A. *et al.* Symmetry and lattice mismatch induced strain accommodation near and away from correlated perovskite interfaces. *Appl. Phys. Lett.* **105**, 131906 (2014).
42. Tebano, A. *et al.* Evidence of Orbital Reconstruction at Interfaces in Ultrathin La_{0.67}Sr_{0.33}MnO₃ Films. *Phys. Rev. Lett.* **100**, 137401 (2009).
43. Lee, J.-S. *et al.* Hidden Magnetic Configuration in Epitaxial La_{1-x}Sr_xMnO₃ Films. *Phys. Rev. Lett.* **105**, 257204 (2010).
44. MacManus-Driscoll, J. L., Suwardi, A. & Wang, H. Composite epitaxial thin films: A new platform for tuning, probing, and exploiting mesoscale oxides. *MRS bulletin* **40**, 933–942 (2015).

Acknowledgements

This work was supported by the European Research Council (ERC) (Advanced Investigator grant ERC-2009-AdG-247276-NOVOX), the Engineering and Physical Sciences Research Council (EPSRC) (Equipment Account Grant EP/K035282/1) and the Isaac Newton Trust (Minute 13.38(k)).

Author Contributions

E.M.C., J.E.K. and J.L.D. contributed equally. The manuscript was written through contributions of all authors. All authors have given approval to the final version of the manuscript.

Additional Information

Supplementary information accompanies this paper at <http://www.nature.com/srep>

Competing Interests: The authors declare no competing financial interests.

How to cite this article: Choi, E.-M. *et al.* Strain-tuned enhancement of ferromagnetic T_C to 176 K in Sm-doped BiMnO₃ thin films and determination of magnetic phase diagram. *Sci. Rep.* **7**, 43799; doi: 10.1038/srep43799 (2017).

Publisher's note: Springer Nature remains neutral with regard to jurisdictional claims in published maps and institutional affiliations.



This work is licensed under a Creative Commons Attribution 4.0 International License. The images or other third party material in this article are included in the article's Creative Commons license, unless indicated otherwise in the credit line; if the material is not included under the Creative Commons license, users will need to obtain permission from the license holder to reproduce the material. To view a copy of this license, visit <http://creativecommons.org/licenses/by/4.0/>

© The Author(s) 2017